Materials Horizons

ROYAL SOCIETY OF CHEMISTRY

COMMUNICATION

View Article Online
View Journal | View Issue

Cite this: *Mater. Horiz.*, 2024, 11, 2206

Received 16th November 2023,
Accepted 19th February 2024

DOI: 10.1039/d3mh01935g

rsc.li/materials-horizons

Fe/Au galvanic nanocells to generate self-sustained Fenton reactions without additives at neutral pH†

Gubakhanim Shahnazarova,[ab] Nour Al Hoda Al Bast,[ab] Jessica C. Ramirez,[ab] Josep Nogues,[ac] Jaume Esteve,[d] Jordi Fraxedas,[a] Albert Serra,[ef] Maria J. Esplandiu *[a] and Borja Sepulveda*[d]

The generation of reactive oxygen species (ROS) *via* the Fenton reaction has received significant attention for widespread applications. This reaction can be triggered by zero-valent metal nanoparticles by converting externally added H_2O_2 into hydroxyl radicals (•OH) in acidic media. To avoid the addition of external additives or energy supply, developing self-sustained catalytic systems enabling onsite production of H_2O_2 at a neutral pH is crucial. Here, we present novel galvanic nanocells (GNCs) based on metallic Fe/Au bilayers on arrays of nanoporous silica nanostructures for the generation of self-sustained Fenton reactions. These GNCs exploit the large electrochemical potential difference between the Fe and Au layers to enable direct H_2O_2 production and efficient release of Fe^{2+} in water at neutral pH, thereby triggering the Fenton reaction. Additionally, the GNCs promote Fe^{2+}/Fe^{3+} circulation and minimize side reactions that passivate the iron surface to enhance their reactivity. The capability to directly trigger the Fenton reaction in water at pH 7 is demonstrated by the fast degradation and mineralization of organic pollutants, by using tiny amounts of catalyst. The self-generated H_2O_2 and its transformation into •OH in a neutral environment provide a promising route not only in environmental remediation but also to produce therapeutic ROS and address the limitations of Fenton catalytic nanostructures.

New concepts

Here we introduce a novel approach based on galvanic nanogenerators to efficiently self-produce, for the first time, significant hydrogen peroxide onsite from water at neutral pH without any additive or energy source to generate reactive oxygen species (ROS) through Fenton pathways. The system relies on Fe/Au hemicells coated with mesoporous silica nanoparticles to generate an exceptional electrochemical driving force. The large surface area of the hybrid nanogenerator enables not only the production and release of H_2O_2 and Fe^{2+} as main ingredients of the Fenton reaction but also the reconversion of the iron cation to maintain an efficient catalytic circuit. These nanogenerators have demonstrated their power through the fast degradation of persistent organic pollutants, in contrast to previous approaches involving external H_2O_2, very low pH levels, and high amounts of catalysts. Therefore, these nanogenerators represent a paradigm shift in Fenton reactions by achieving the degradation of chemical species at neutral pH without external additives and utilizing ultralow amounts of catalytic nanomaterial. Beyond the degradation of water contaminants, these nanomaterials are promising for the targeted therapeutic generation of ROS, emphasizing the importance of neutral pH conditions. Furthermore, their ability to produce valuable chemicals, such as H_2O_2, positions them as a transformative strategy with far-reaching implications.

Introduction

Reactive oxygen species (ROS) are highly reactive free radicals with a wide range of applications, spanning from the removal of organic pollutants to the destruction of cancer cells.[1–5] One mechanism to efficiently generate ROS is the Fenton reaction, which uses H_2O_2 and transition metal cations as catalysts (*e.g.*, Fe^{2+}, Cu^{2+}, Ag^{+}) for generating highly oxidant hydroxyl radicals (•OH). The interest in the Fenton reaction has increased with the development of highly reactive zero-valent metal nanoparticles (*e.g.*, iron, silver, copper and aluminum),[6–8] which can efficiently generate metal cations through their corrosion in water media, as a result of the electron transfer between the metals and O_2.[9] Iron nanoparticles are the most widely studied materials due to their low cost, low toxicity, abundance, and reducing activity.[8,10–12]

[a] *Catalan Institute of Nanoscience and Nanotechnology (ICN2), CSIC and BIST, Campus UAB, Bellaterra, E-08193 Barcelona, Spain. E-mail: mariajose.esplandiu@icn2.cat*
[b] *Universitat Autònoma de Barcelona, 08193 Cerdanyola del Vallès, Barcelona, Spain*
[c] *ICREA, Pg. Lluís Companys 23, 08010 Barcelona, Spain*
[d] *Instituto de Microelectrónica de Barcelona (IMB-CNM, CSIC), Barcelona, 08193, Spain. E-mail: borja.sepulveda@csic.es*
[e] *Grup d'Electrodeposició de Capes Primes i Nanoestructures (GE-CPN), Departament de Ciència de Materials i Química Física, Universitat de Barcelona, Martí i Franquès, 1, E-08028, Barcelona, Catalonia, Spain*
[f] *Institute of Nanoscience and Nanotechnology (IN2UB), Universitat de Barcelona, Barcelona, Catalonia, Spain*

† Electronic supplementary information (ESI) available. See DOI: https://doi.org/10.1039/d3mh01935g

Zero-valent iron nanoparticles (nZVI) are highly reactive reagents that can trigger different reaction pathways, such as redox, adsorption, or precipitation, depending on the reaction conditions.[13] Despite the merits of nZVI in Fenton reactions and other reaction pathways, they exhibit important limitations. For instance, nZVI can easily aggregate in solution due to magnetic and electrostatic interactions, decreasing their reaction performance.[14] Different support materials, such as silica or metal–organic frameworks, can be used to overcome such limitations and increase their stability and reactivity.[15,16] Another drawback is their short lifetime due to the surface passivation of the nZVI system over time caused by the formation of oxyhydroxides or oxides that hinder the electron transfer from the Fe^0 core to the surface. Such a problem is intensified at higher pH, thus limiting the Fe nanoparticle activity to a narrow acidic pH range.[17–19] The surface passivation can restrict the nZVI applications in environmental remediation when the redox process is the main decontamination pathway. However, the passivated iron nanoparticles can also be exploited for pollutant adsorption and co(precipitation) through chemisorption and electrostatic interactions.[20]

To simplify the Fenton reaction with zero-valent nanoparticles, new strategies to minimize the need for external additives (*e.g.*, H_2O_2) or energy supplies (*e.g.*, UV light, ultrasounds) are needed. The capability to produce H_2O_2 *in situ* is therefore very relevant for activating Fenton or Fenton-like processes to generate ROS with higher oxidizing power.[21] However, the majority of the Fenton nZVI systems have relied on the external supply of H_2O_2 to achieve proper ROS generation, which reflects the difficulties in tuning the reactivity of the nZVI/O_2 system due to the many dependent reaction parameters. Different strategies have been proposed to improve the nZVI systems, such as introducing other metals or components into the nZVI system to create inter-metallic galvanic cells that enhance iron reactivity. The galvanic effect is induced when two metals with different electrochemical potentials are brought into contact, forming a pair of electrodes, acting as the cathode and anode.[22–25] The galvanic effect has been used for a variety of purposes, including cathodic protection,[26–30] which involves using a sacrificial metal as the anode to protect a more valuable metal acting as the cathode. However, the galvanic effect could also be applied to boost the reactivity of the anodes for efficient generation of ROS. There are some examples of ZVI-based systems that use the galvanic effect to trigger reductive decomposition or Fenton oxidation of analytes, such as Fe-based metallic glasses, high entropy alloys, and bi-component systems. Fe-based metallic glass catalysts (*e.g.*, FeB, FeBC, FeBP, FeSiB, FePC, FeSiBCu, and FeNbSiB) feature high density of reactive sites due to the formation of local nanosized galvanic cells between different Fe-rich and Fe-poor atomic clusters, which promote the rapid degradation of dyes.[31–39] On the other hand, Fe-based high entropy alloys are typically made by mixing Fe with roughly equal amounts of multiple metallic elements, such as Cu, Co, Cr, Ni, Mn, *etc.* The resulting materials have been mainly exploited for dye decomposition through reductive pathways.[40] Finally, bi-component systems integrating Fe with Co, Ni, Cu, Pt, Pd, or carbon have also been studied for the reductive trapping of heavy ions or the reductive degradation of organic contaminants.[41–45] However, very few studies have demonstrated the Fenton-like pathway for analyte oxidative decomposition. Moreover, in most systems, external addition of H_2O_2 was required, as the *in situ* generation of H_2O_2 was insufficient to stimulate the generation of $^{\bullet}OH$ radicals. The very few cases that produce *in situ* sufficient H_2O_2 for activating the ROS production were under acidic medium conditions (pH ~ 3) or using very large catalyst dosages.[46–48]

Here, we present novel highly reactive Fe/Au galvanic nanocells (GNCs) to generate Fenton reactions, achieved by merging the large electrochemical potential difference between the Fe and Au and their high surface area. This catalytic system is fabricated by depositing a Fe/Au bilayer on an array of self-assembled porous silica nanoparticles. The Fe/Au GNCs enable simultaneous efficient release of Fe^{2+} and generation of H_2O_2 to trigger the production of ROS *via* the Fenton reaction without the need for any external chemical additives or energy sources. Moreover, in contrast to previous Fe-based systems, the Fe/Au GNCs are highly efficient at neutral pH, requiring very low amounts of catalyst, as demonstrated by the rapid degradation and mineralization of relevant organic pollutants, like the dye methylene blue and the antibiotic tetracycline.

Results and discussion

Fabrication of the Fe/Au galvanic nanocells

The Fe/Au galvanic nanocells for Fenton generators consisted of arrays of self-assembled large-pore nanoporous silica nanoparticles (diameter 200–250 nm, pore size 35 nm) (Fig. S1, ESI†) on which Fe (60 nm) and Au (20 nm) layers were deposited by electron beam evaporation, forming a rough bimetallic semi-shell (Fig. 1a and Fig. S2, ESI†). The nanoporous silica nanoparticles acted as a high surface area support to increase the reactivity to the bimetallic coverage. In addition, the highly hydrophilicity of the silica matrix enabled efficient water penetration and, therefore, direct contact of water to both metals.

To assess the reaction mechanisms of the Fe/Au GNCs, similar structures composed only of a zero-valent Fe layer (60 nm thick) (Fig. S3, ESI†) and structures with different Fe and Au thickness and position were also studied.

The experiments were conducted using the Fe/Au or Fe nanostructured layers attached to silicon substrates to enable monitoring the fast reaction, which was triggered as soon as the samples were immersed in water. This approach also provided a quick and simple strategy for the recovery of the catalyst. The morphology of the Fe/Au GNCs can be observed in Fig. 1b, c and Fig. S4 (ESI†), showing the obtained metallic Fe and Au semi-shell layers on the porous silica nano-particles. Importantly, this fabrication method enabled depositing the metallic Fe and Au layers without any interlayer passivation.

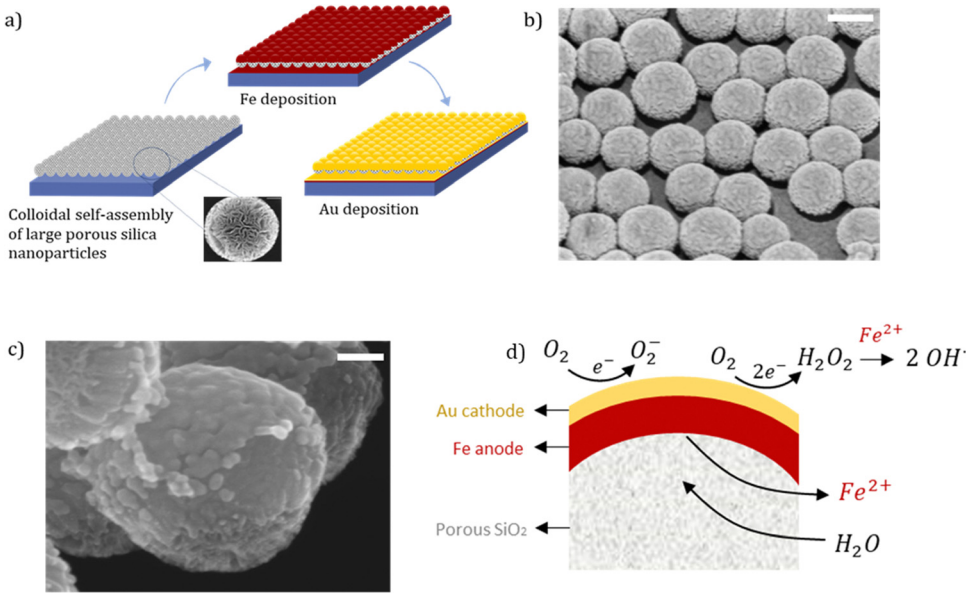

Fig. 1 (a) Schematic of the fabrication process of the Fe/Au galvanic nanocells to generate the Fenton reaction, starting with the self-assembly of the large pore silica particles on a silicon substrate and the subsequent physical vapor deposition of the Fe and Au layers on top. The inset shows a scanning electron microscopy (SEM) image of one porous silica particle (250 nm); see Fig. S1 (ESI†). (b) SEM image of the self-assembled Fe/Au GNCs (scale bar 200 nm). (c) SEM image of Fe/Au GNCs (scale bar 50 nm). (d) Schematic depicting the galvanic Fe/Au reaction mechanism, showing the main reactions pathway to trigger the Fenton reaction.

Galvanic reaction pathway

The working principle of the Fe/Au GNCs for ROS generation *via* the Fenton reaction is shown in Fig. 1d. The galvanic cell is initiated by the difference in electrochemical potentials established at the different interfaces: Fe/Au, Au/electrolyte, and Fe/electrolyte. Part of the differences in the electrochemical potentials arises from the large difference in the work function (Φ) between Fe and Au metals (Φ_{Fe}= 4.65 eV, and Φ_{Au} = 5.32 eV).[49] When Fe and Au come into contact, the substantial difference in work functions induces electron transfer from Fe to Au, resulting in the charging of these materials (Fe becomes positively charged and Au becomes negatively charged), thus creating a significant potential difference at the interface. This effect influences the electrochemical potentials at both metal/liquid interfaces when immersed in water, promoting their discharge through redox reactions. At the Fe/liquid interface, discharge occurs by releasing Fe^{2+} ions while transferring the electrons into the Au metal, driven by the lower Fe nobility, ($E^0_{Fe^{2+}/Fe}0 = -0.44$ V), thus making Fe the anode. On the Au side, the discharge is achieved through electron donation to species in the solution inducing reduction processes within the solution. In this case, Au acts as an electron intermediary, receiving electrons from the Fe interface and donating them to the solution provided by its high nobility ($E^0_{Au^+/Au^0}$ = + 1.83 V) and thus acting as the cathode. These charge transfers affect the electrochemical potentials at the different interfaces and contribute to a global and large electrochemical difference that sustains an enhanced redox rate and Fe corrosion over time. There are two possible reaction pathways with the electrons transferred to the Au layer. The electrons can reduce the oxygen available in the water to superoxide radicals, which can then undergo several steps to produce H_2O_2. Alternatively, the electrons transferred to the cathode can directly produce H_2O_2. Finally, the released Fe^{2+} cations decompose the produced H_2O_2 to generate the hydroxyl radicals, thus triggering the Fenton cycle. Therefore, in the Fe/Au GNCs, the Fe layer can be considered as a reactant that is consumed over time, while the Au layer acts as a catalyst for oxygen reduction.

To validate this reaction pathway, the self-generation of the main ingredients needed to trigger the Fenton reaction was first identified by monitoring the H_2O_2 production and the release of Fe^{2+} during the spontaneous reaction of the GNCs in water at pH 7. The detection of the produced H_2O_2 is complex due to its short lifetime, as it undergoes a fast reaction with the iron cations. Moreover, most conventional techniques have high detection limits (about mg L^{-1}) or require very acidic medium conditions.[46,50,51] To overcome these challenges, we adapted a procedure for detecting H_2O_2 that has been used in biological samples,[52] which relies on an enzymatic reaction to generate a fluorescent probe of H_2O_2, whose emission intensity is proportional to the H_2O_2 concentration. Briefly, H_2O_2 was detected using the Amplex™ Red reagent (10-acetyl-3, 7-dihydroxyphenoxazine), which is an extremely sensitive peroxidase substrate in the presence of the enzyme horseradish peroxidase (HRP), to produce highly fluorescent resorufin (see the ESI† and Fig. S5). As an additional advantage, this approach enables collecting the fluorescence signals at the nanostructured interface using confocal fluorescence microscopy.

Fig. 2a shows the intensity of the fluorescence emission spectra of resorufin for the Fe/Au GNCs compared to the Fe system. The much higher intensity of the resorufin fluorescence signal confirmed the enhanced *in situ* production of

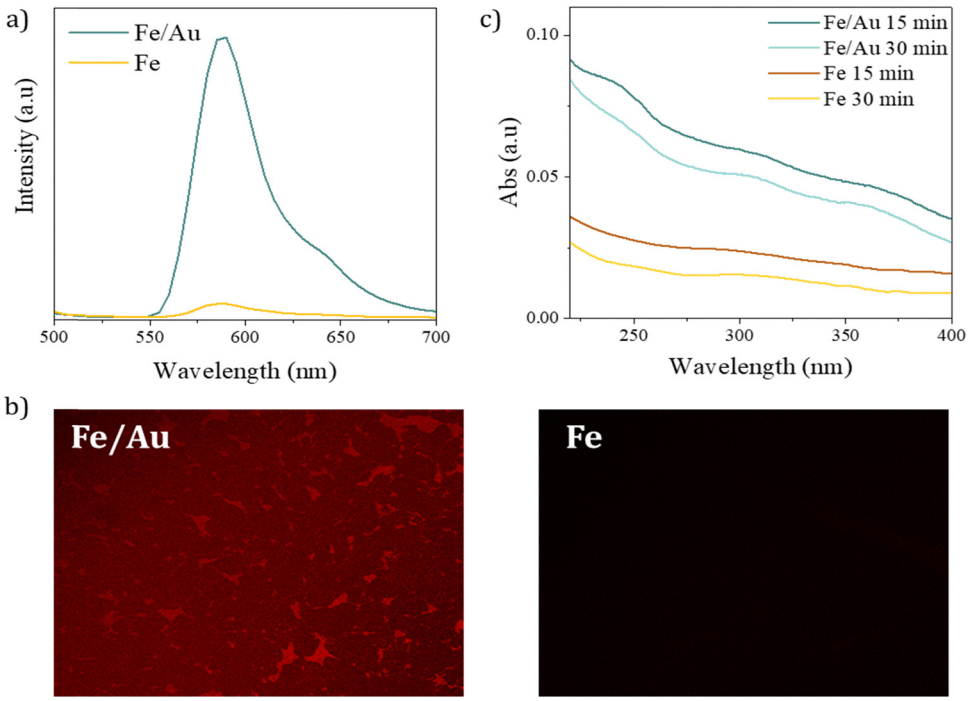

Fig. 2 (a) Fluorescence emission of resorufin for the Fe/Au and Fe nanostructures excited at 488 nm. (b) Fluorescence images of the Fe/Au and Fe nanostructured surfaces, respectively. (c) UV absorbance of the reaction fluid for the Fe/Au and Fe nanostructures after 15 and 30 min of reaction (for the detection of Fe ions), respectively.

H_2O_2 in the Fe/Au galvanic nanocell, whereas it was minimal for the Fe counterpart. After the first ten minutes of reaction, the H_2O_2 concentration was remarkably higher (36-fold) in the Fe/Au nanostructures (1.8 μM) compared to the Fe nanostructures (0.05 μM). This effect was clearly confirmed by the drastically enhanced intensity in the confocal images of the Fe/Au nanostructures compared to the Fe nanostructures (Fig. 2b).

In the Fe/Au GNCs, the release of Fe^{2+} cations can be performed either directly from the rims of the Fe/Au semishells, in which the Fe layer is not completely covered by Au, or through the porous and highly hydrophilic silica matrix. The Fe cations release in water was evaluated *via* ultraviolet (UV) spectroscopy by detecting their absorption below 300 nm,[53] after immersing the Fe/Au and Fe systems in water. Interestingly, as illustrated in Fig. 2c, the amount of the released Fe ions by the Fe/Au nanostructures was significantly higher than that of the Fe counterpart after the different reaction times, despite the substantially lower iron surface in direct contact with water. The enhanced release of Fe ions was a direct result of the galvanic effect. It is important to point out that the Fe ions concentration in water can, in some cases, decrease over longer reaction times due to the formation of precipitates either in the solution or on the nanostructured surfaces, which could decrease the Fe ion absorbance observed in Fig. 2c for longer reaction times. The galvanic enhanced release of iron cations was further confirmed and quantified *via* ICP-mass spectroscopy, showing concentrations of 430 ppb and 8 ppb for the Fe/Au and Fe nanostructures, respectively, during the first 15 minutes of reaction.

However, these measurements cannot distinguish the oxidation state of the released ions. To sustain the Fenton reaction, the reduction of the Fe^{3+} ions into Fe^{2+} is crucial (see the reaction scheme in the discussion). Therefore, to assess the capacity of the galvanic generators to keep a high concentration of Fe^{2+} ions necessary to sustain the Fenton reaction, additional studies were conducted to discriminate and quantify the ratio of Fe^{2+} and Fe^{3+} ions generated. We used a spectrophotometric assay based on the ability of Fe^{2+} ions to form colored complexes with phenanthroline. As described in the ESI,† a calibration curve for the Fe^{2+}/phenanthroline complex was prepared (Fig. S6b, ESI†) and subsequently used to determine the Fe^{2+} concentration produced by the Fe/Au and Fe nanostructures after complexing the ion release samples with phenanthroline (see the absorbance measurements in Fig. S6c, ESI†). The Fe^{3+} concentration was then calculated by converting the total iron ion released from the reactors into Fe^{2+} by the hydroxylamine reducing agent, complexing it with the phenanthroline, and subtracting the result from the previously obtained Fe^{2+} concentration. The Fe^{2+} and Fe^{3+} concentrations were 1.56×10^{-6} M and 0.76×10^{-6} M, respectively, for the Fe/Au nanostructures. Meanwhile, for the Fe nanostructures, the Fe^{2+} and Fe^{3+} concentrations were 1.7×10^{-7} M and 4.5×10^{-7} M, respectively. Consequently, in the case of the Fe/Au system, the concentration of Fe^{2+} ($[Fe^{2+}]$) constituted 68% of the total iron ions ($[Fe^{2+}] + [Fe^{3+}]$), whereas it was only 27% for the pure Fe system. This result highlights the importance of the Au layer to recycle the Fe^{3+} ions by reducing them to Fe^{2+}. This process is crucial to sustain the Fenton reaction and to increase the ROS

production and reactivity. In addition, the total concentration of Fe^{2+} was *ca.* 10-fold larger in the galvanic Fe/Au system, despite the coverage of the Fe layer by the Au layer. However, we have not observed the complete release of the Fe layer, which could point towards final Fe passivation that stops the reaction.

These results reveal that the Fe/Au galvanic nanocells can effectively produce the fundamental ingredients (H_2O_2 and Fe^{2+} ions) to trigger the Fenton catalytic pathway with high efficiency in water at neutral pH without any external additives.[54]

Catalytic activity

To demonstrate the additive-free Fenton reaction in water at neutral pH, the catalytic activity of the Fe/Au and Fe nanostructures was evaluated for the degradation and mineralization of two typical non-biodegradable environmental pollutants,[55,56] methylene blue (MB) and tetracycline (TC). Importantly, the catalytic tests were conducted using very low concentrations of Fe/Au and Fe nanostructures of 14.8 μg mL^{-1} and 14 μg mL^{-1}, respectively.

The degradation and mineralization of MB (10 ppm, 3.2 mg L^{-1}) were analyzed by the decrease of its UV-VIS spectra (absorbance peak centered at 664 nm) and the quantification of the total organic content (TOC), respectively. As shown in Fig. 3a and b, the MB degradation was extremely fast for the Fe/Au nanostructures, with an almost complete degradation in the first 15 min, compared to the substantially lower kinetics of the Fe nanostructures. This clearly indicates the enhanced reactivity conferred by the galvanic cell formed between the Fe and Au layers.

The kinetics of the MB removal process (Fig. 3c) exhibited a pseudo first-order kinetics for both Fe/Au and Fe nanostructures, following the equation $C_t = C_0 e^{-kt}$, where C_t represents the contaminant concentration at time t, C_0 is the initial concentration, and k is the first-order kinetic reaction rate constant. The k values of the Fe/Au and Fe systems were 0.16 min^{-1} and 0.032 min^{-1}, respectively. Therefore, the Fe/Au GNCs had a 5-fold higher reaction rate compared to the bare Fe nanostructures.

Considering the fast MB degradation kinetics by the Fe/Au nanostructures, we analyzed the degradation and mineralization after only 15 min of reaction (Fig. 3d). After this short period, the Fe/Au nanostructures achieved 74.8% degradation *versus* 32.6% by the Fe counterpart. A similar trend was observed in the mineralization rate, reaching 64.4% and 19.7% for the Fe/Au and Fe nanosystems, respectively, thereby confirming the efficient ROS generation by the galvanic effect. To achieve a similar degradation level, the Fe nanostructures required *ca.* 70 min of reaction. For longer reaction times (90 min), both systems could reach high degradation and mineralization values, with degradation efficiencies of 94.0% and 86.3% for Fe/Au and Fe nanostructures, respectively (Fig. 3f), while the mineralization reached 86.1% and 81.1%, respectively.

The Fe/Au GNCs did not suffer any significant morphologic change after the 90 min reaction (Fig. S7a, ESI†), which highlights the stability of the deposited Fe/Au layer on the porous silica nanoparticles. However, to analyze the oxidation state of the Fe and Au layers before and after the galvanic reaction, XPS experiments were carried out for the configurations in which

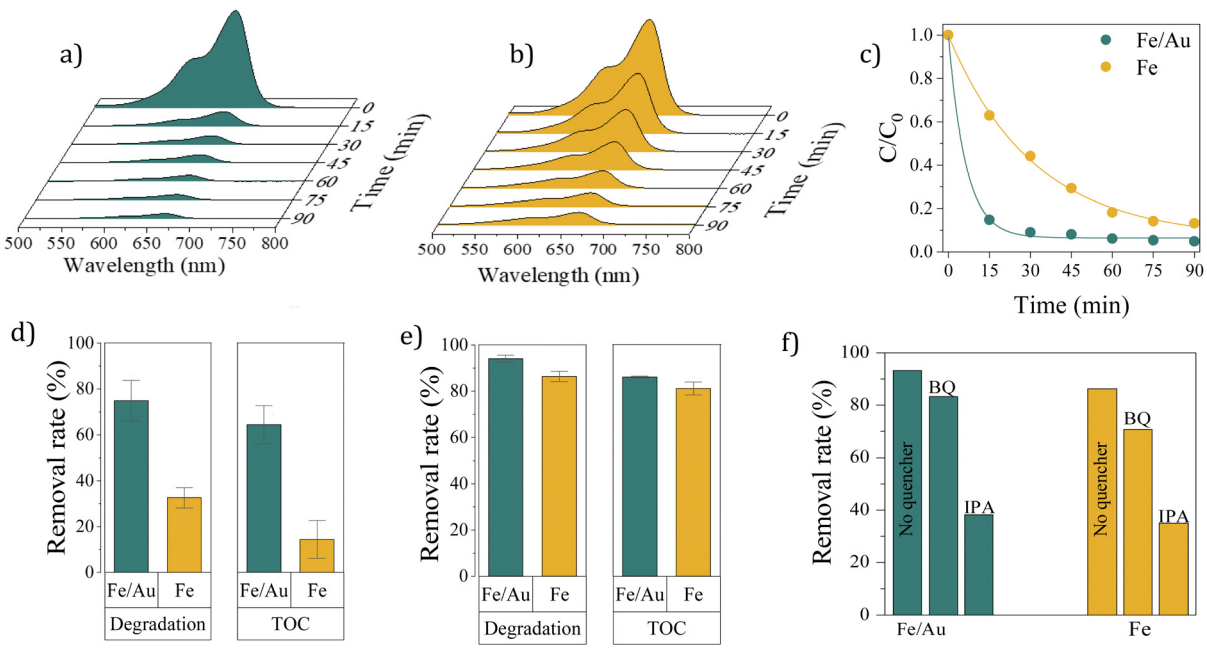

Fig. 3 Catalytic degradation of MB in the presence of (a) Fe/Au and (b) Fe nanostructures. (c) Comparison of the reaction kinetics for the MB degradation and their fittings through pseudo-first order-nonlinear kinetics ($R^2_{Fe/Au}$ = 0.998, R^2_{Fe} = 0.997). (d) and (e) Degradation and TOC removal rates after 15 min and 90 min of reaction, respectively. (f) MB degradation rate in the presence of the ROS quenchers benzoquinone (BQ) and isopropanol (IPA) for the Fe/Au and Fe nanostructures after 90 min of reaction.

either the Au or Fe layers were on top (Fig. S7b, ESI†). The first relevant result is that the Au layer was not oxidized during the galvanic process and preserved the metallic state when it was located at the top, whereas there was slight oxidation when Au was at the bottom, probably due to the higher nanostructuration of the Au layer at the rims when deposited directly onto porous SiO_2 nanoparticles (Fig. S4a and b, ESI†). These gold nanostructures at the rims could be more reactive, and some of these nanoparticles could also be uncovered from the upper Fe layer in this region, making Au more susceptible to ROS, considering that iron provides electrons to gold when they are in contact, helping to protect Au from ROS oxidation. In the case of the Fe layer before the reaction, the XPS signal was negligible when Fe was covered by Au, as this layer completely screened the XPS signal. In contrast, after the reaction with MB for 90 min, there was a clear signal of the oxidized Fe (mainly Fe^{3+}), which can be attributed to the Fe cations that were released to water during the galvanic process and deposited on the Au surface during the degradation and drying processes. In contrast, when the Fe layer was on top, the XPS signal corresponded to metallic iron and essentially Fe^{3+}. No significant differences could be observed between the two analyzed systems for discriminating the contribution of Fe^{2+}, although a slightly higher Fe^{2+} content can be observed in the sample with the Fe film on top.

To determine the influence of Fe and Au thickness on reactivity, MB degradation tests for the following configurations were carried out: Fe 20 nm/Au 20 nm; Fe 40 nm/Au 20 nm; Fe 60 nm/Au 20 nm, and Fe 60 nm/Au 10 nm (Fig. S8 a and b, ESI†). These assays showed a significant decrease in the degradation efficiency when either the Fe or Au layers' thickness was reduced. The reactivity reduction with the Fe thickness is consistent with the fact that the Fe layer is a reactant that is consumed during the process. In contrast, the reactivity decrease with the lower Au thickness can be due to the poor coverage of the Fe layer for very thin films, particularly on rough and high curvature surfaces, such as those of the porous SiO_2 layers, thereby enabling a fast passivation of the Fe layer.

Moreover, to determine the effect of the Fe and Au layers' position, we compared the reactivity of the GNCs when either the Au or Fe layers were positioned on top (Fig. S8c, ESI†). The results showed that the Au/Fe galvanic nanocells (Fe on top) exhibited a substantially lower degradation efficiency compared to the Fe/Au nanocells (Au on top). This effect could be attributed to the fast passivation of the Fe layer when it is in direct contact to water. In addition, when the Au layer is at the bottom, the generated ROS go through the porous silica matrix and can be easily deactivated due to their short life times, thereby contributing to reduced reactivity. Therefore, the Au protection of the Fe layer is key to ensure the adequate generation of the Fenton reaction at pH 7 and without any additives.

To further confirm the Fenton reaction pathway and the generated ROS species, radical quenching experiments were performed. To this end, isopropanol and benzoquinone were used as quenchers of hydroxyl ($^{\bullet}OH$) and superoxide ($^{\bullet}O_2^-$) radicals, respectively. As shown in Fig. 3f, when isopropanol was added to the reaction solution, the MB degradation efficiency declined distinctly to 38.3% and 35.0% for the Fe/Au and Fe systems, respectively. However, after adding the benzoquinone superoxide scavenger, the MB degradation efficiency only slightly decreased to 83.2% and 70.8% for Fe/Au and Fe nanostructures, respectively. These results corroborated that the main reactive species for the MB removal were hydroxyl radicals, with superoxide radicals playing a secondary role, as expected from the Fenton reaction pathway.

So far, all the experiments were performed with the oxygen naturally dissolved in water upon contact with air. To show the importance of the oxygen dissolved in water, measurements of the catalytic activity of these nanostructures were also performed in a controlled argon atmosphere using MB. Degradation efficiencies of only 44% and 48% were found for Fe/Au and Fe nanostructures, respectively, after 90 minutes of reaction (see degradation curves in Fig. S9, ESI†). As expected, a decrease in the degradation rate was observed due to the absence of oxygen dissolved in the solution, and consequently, to the lack of H_2O_2 production. The limited degradation activity could potentially be attributed to the presence of residual traces of oxygen in the solution. However, we cannot rule out other degradation mechanisms, such as reductive degradation or the generation of ROS *via* possible *in situ* oxygen generation through heterogeneous catalysis involving metal surface hydroxides. It is well-documented that under neutral pH conditions and in the absence of oxygen, the most likely reaction is the formation of hydrogen gas and hydroxide ions ($Fe + H_2O \rightarrow H_2 + OH^-$).[57] The produced hydroxide ions can be adsorbed onto the metallic surface of metals, promoting the generation of oxygen in the anodic regions of iron. In line with this, there are many studies on iron-based electrocatalysts that promote oxygen evolution reactions *via* hydroxides.[58–61] In that case, the reaction kinetics would be significantly slower, which explains the low degradation rate in the absence of oxygen, particularly affecting the Fe/Au system. Furthermore, the catalytic activity was also assessed in the presence of oxygen-saturated water through oxygen bubbling. In this case, almost no MB degradation was observed in either of the systems, primarily due to rapid iron passivation.

To show the strength and versatility of the Fe/Au GNCs, their high reactivity was also demonstrated by the degradation and mineralization analysis of the pollutant tetracycline (40 ppm, 17.7 mg L^{-1}), again at neutral pH and without the addition of H_2O_2 (Fig. 4a and b). The absorbance spectra of TC significantly decreased (72.3%) in the presence of the Fe/Au nanostructures (Fig. 4c). In contrast, the Fe nanostructures showed poor performance towards TC degradation, with only 33.6% removal (Fig. 4c). These results were correlated with the obtained mineralization efficiencies of 69.4% and 29.4% for Fe/Au and Fe nanostructures, respectively (Fig. 4d). In addition, the kinetic constants were estimated to be 0.081 min^{-1} and 0.013 min^{-1} for Fe/Au and Fe nanostructures, respectively (Fig. 4e), thereby demonstrating the higher reactivity of the GNCs.

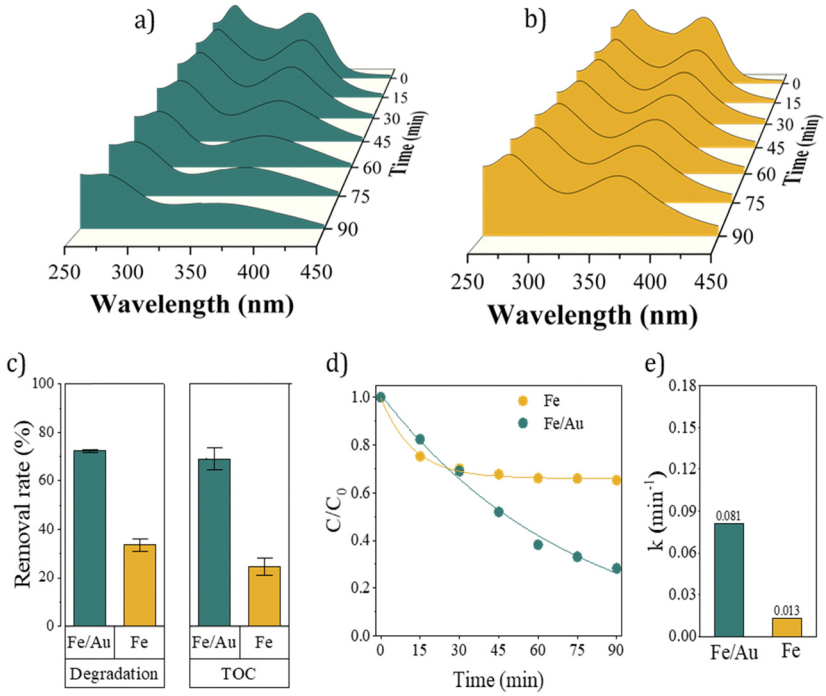

Fig. 4 TC degradation in the presence of the (a) Fe/Au and (b) Fe nanostructures. (c) Degradation and TOC removal rates. (d) Comparison of kinetic fitting of TC decay through pseudo-first order-nonlinear kinetics ($R^2_{Fe/Au}$ = 0.996, R^2_{Fe} = 0.992) and (e) the corresponding reaction rates (*k*).

Discussion

The comparative degradation studies of MB and TC clearly indicate the enhanced performance of Fe/Au with respect to Fe catalytic nanostructures, which is ascribed to the galvanic cell formation in the bimetallic system. The electrochemical potential difference between both metals is the driving force to accelerate iron oxidation and the transfer of the released electrons to the Au region for the efficient reduction of O_2 to H_2O_2. The *in situ* generation of iron cations and H_2O_2 is the basic ingredient for triggering the generation of $^{\bullet}OH$ and Fe^{2+} as outlined in the chemical equations below.

$$Fe^0 + O_2 + 2H^+ \rightarrow Fe^{2+} + H_2O_2 \quad (1)$$

$$Fe^{2+} + H_2O_2 \rightarrow Fe^{3+} + {}^{\bullet}OH + OH^- \quad (2)$$

$$Fe^{3+} + H_2O_2 \rightarrow Fe^{2+} + {}^{\bullet}HOO + H^+ \quad (3)$$

$$Fe^0 + 2Fe^{3+} \rightarrow 3Fe^{2+} \quad (4)$$

$$Fe^{3+} + e^- \xrightarrow{Au} Fe^{2+} \quad (5)$$

Therefore, the hydroxyl radicals play a key role in degrading the organic pollutants. However, an efficient regeneration of Fe^{3+} to Fe^{2+} is also key to sustaining the redox catalytical loop and the efficacy of the degradation process. In the absence of Au, the Fe^{3+} reduction is mainly accomplished with the released electrons at the Fe^0 interface. However, it is known that the iron cations, and particularly Fe^{3+}, can easily hydrolyze water and form iron hydroxides or react with oxygen to form oxides, which passivate the metallic iron over time, thus hindering the electron transfer and mass transport of reagents and products. The efficacy of the high-driving force galvanic cell to channel electrons into the Au layer also creates a source of electrons for the regeneration of Fe^{3+} into Fe^{2+} [eqn (5)], leading to an enhancement in the reconversion rate of Fe^{2+}/Fe^{3+}. Indeed, signatures of the enhanced Fe^{2+} production at the Fe/Au nanostructures were observed through spectrophotometry, where 68% of the iron cations in the solution were in the form of Fe^{2+} in the Fe/Au system, whereas only 27% were observed for the Fe nanostructures. This result reinforces the claim of an enhanced ion reconversion rate at the heterogenous galvanic cell. The increased recovery rate of the Fe^{2+} helps to efficiently sustain the Fenton cycle while minimizing the side reactions of the formation of iron hydroxides/oxides at the iron surface. The acceleration of Fenton-type reactions also led to more complete degradation of the organic compounds, with fewer by-products being produced, as proved by the TOC mineralization analysis.

Another benefit of using the Fe/Au galvanic system is the capacity to operate the reaction at neutral pH. Generally, Fe-based catalysts show their optimum activity at acidic pH (~3). Increasing the pH significantly decreases the activity of the Fe-based systems due to the formation of the hydroxide/oxide passivating layers. In contrast, the Fe/Au nanostructures can operate at a more neutral pH while maintaining their high catalytic activity. This effect can be ascribed to the accelerated Fenton reaction process and the fast iron cation reconversion through the high reducing power of the Au layer. This effect allows the ROS-mediated degradation reaction being the dominant pathway and minimizing the occurrence of competing side reactions.

To contextualize the performance of the catalytic Fe/Au GNCs with respect to other Fenton galvanic cells reported in

Table 1 Comparison of the reported studies with Fenton galvanic cells for the degradation of MB and TC together with the results of this work

Catalyst	Catalyst dosage	[MB]	H_2O_2 supply	pH	D.E.	k (min^{-1})	k_{norm} (min^{-1} g^{-1})
Methylene blue (MB) removal							
Fe/Au[a]	0.015 g L^{-1}	3.2 mg L^{-1}	No	7	94.6%	0.16	*10.6*
Fe[a]	0.014 g L^{-1}	3.2 mg L^{-1}	No	7	86.3%	0.032	2.3
Fe/CNTs plates[46]	—	20 mg L^{-1}	No	3	—	0.0852	—
Fe/C[66]	**1.25 g L^{-1}**	—	**57 mM**	**3**	100%	—	—
Fe/C[66]	**1.25 g L^{-1}**	—	No	**3**	<20%	—	—
Fe/Ni[67]	**2 g L^{-1}**	600 mg L^{-1}	**50 mM**	**4.76**	61.4%	0.022 (303 K)	0.011
Fe/Ni[67]	**2 g L^{-1}**	1000 mg L^{-1}	No	**4.76**	30.8%	0.012 (303 k)	0.006
Methylene blue (MB) removal using amorphous alloys							
FeBC[33]	**0.5 g L^{-1}**	20 mg L^{-1}	**0.2 mM**	**3.5**		0.16	0.32
FeSiB[35]	**0.5 g L^{-1}**	100 mg L^{-1}	**1 mM**	**3**	95%	0.37	0.74
FePC[35]	**0.5 g L^{-1}**	100 mg L^{-1}	**1 mM**	**3**	95%	0.56	1.12
FeB[37]	**0.5 g L^{-1}**	20 mg L^{-1}	**1 mM**	**3**	—	0.302	0.60
FeSiB[37]	**0.5 g L^{-1}**	20 mg L^{-1}	**1 mM**	**3**	—	0.111	0.22
FeSiBPNbCu[31]	**2.4 g L^{-1}**	60 mg L^{-1}	**0.1 M**	—	67.76%	0.018 (353 K)	0.008
FeSiBPNbCuNi[31]	**2.4 g L^{-1}**	60 mg L^{-1}	**0.1 M**	—	99.99%	0.065 (353 k)	0.027
FeBC[68]	0.05 g L^{-1}	20 mg L^{-1}	**2 mM**	**3**	—	0.19 (298 K)	3.8
FeBP[68]	0.05 g L^{-1}	20 mg L^{-1}	**2 mM**	**3**	—	0.13 (298 K)	2.6
FeSiB[34]	0.5 g L^{-1}	20 mg L^{-1}	**1 mM**	**3**	~43% (Mineralization)	0.692	1.38
FeSiBCuNb[34]	0.5 g L^{-1}	20 mg L^{-1}	**1 mM**	**3**	~20% (Mineralization)	0.099	0.198
FePCCu[39]	0.5 g L^{-1}	100 mg L^{-1}	**1 mM**	**3**	—	0.34	0.608
FeCoPCCu[39]	0.5 g L^{-1}	100 mg L^{-1}	**1 mM**	**3**	—	0.47	0.94
FeCrNbYB[32]	0.5 g L^{-1}	100 mg L^{-1}	**2 mM**	**3**	—	0.182 (303 K)	0.364
FeSiB[36]	0.05 g L^{-1}	20 mg L^{-1}	**1 mM**	**3**	—	0.9	*18*
Tetracycline (TC), oxytetracycline (OT) and chlortetracycline (CTC) removal							
Fe/Au[a]	0.015 g L^{-1}	TC 17.7 mg L^{-1}	No	7	72.3%	0.081	*5.4*
Fe[a]	0.014 g L^{-1}	TC 17.7 mg L^{-1}	No	7	33.6%	0.013	0.93
Fe/Cu[69]	**1.2 g L^{-1}**	TC 8 μg L^{-1}	**2 g L^{-1}**	7	85.1%	—	
Fe/Cu/C[70]	**0.5 g L^{-1}**	CTC 50 mg L^{-1}	No	**3.6**	70.7%	0.294	0.59
Fe/Cu[71]	**5 g L^{-1}**	TC 50 mg L^{-1}	**50 mM**	**3**	97%	1.122	0.22
Fe/Pd/rGox[48]	**0.1 g L^{-1}**	OT 100 mg L^{-1}	No	**5**	96.5%	0.056	0.56
Fe/Pt[47]	**0.5 g L^{-1}**	OT 100 mg L^{-1}	No	**5**	99.2%	—	—
Fe/Cu[41]	**0.2 g L^{-1}**	OT 100 mg L^{-1}	No	**5–6**	71.4%	—	—
Fe/Ni[41]	**0.2 g L^{-1}**	OT 100 mg L^{-1}	No	**5–6**	62.3%	—	—

[a] This work. D.E.: degradation efficiency.

the literature, Table 1 has been included. The table collects various parameters of different studies addressing the degradation of MB and TC (*e.g.*, catalyst dosage, external H_2O_2 supply, pollutant concentration, degradation efficiency, and reaction rate constants). The normalized rate constants (k_{norm}) with respect to catalyst dosage have also been indicated for easier comparison. The cells in the table that are colored blue indicate the use of external H_2O_2, acidic pH conditions, or large amounts of catalyst (>0.05g L^{-1}). The cells highlighted in yellow indicate normalized rate constants above 5. The table also includes the reaction conditions and results obtained using the Fe/Au and Fe nanostructures of the current work.

While MB has been extensively studied using other galvanic systems, there have been very few studies on the degradation of TC using Fenton galvanic cells. Most of the studies on TC involve the removal of antibiotics, primarily through adsorption. Therefore, we have also included studies on derivatives of TC, such as oxytetracycline (OT) and chlortetracycline (CTC).

In the case of MB, the reported studies required either an external supply of H_2O_2 or the maintenance of highly acidic conditions (pH ~ 3), or a high catalyst dosage. One of these studies stands out due to its very high normalized rate constant of 18, which was achieved through a complex pretreatment of the catalyst involving high annealing temperatures and ball milling, in addition to the use of external H_2O_2 or the adjustment of the operating pH to 3. With respect to TC degradation, most of the studies were performed under more acidic conditions and using large dosage of catalysts.

Under this comparative context, the galvanic reactors reported in this work exhibited a very relevant improved degradation performance for both MB and TC under very mild conditions at which the other reported systems are ineffective. These results emphasize the benefits of the Fe/Au GNCs due to their capability to produce *in situ* sufficient H_2O_2 to trigger the Fenton reaction. This has been achieved by forming a galvanic cell with a high driving force and a large surface area that allows operation at neutral pH and with a very low amount of catalysts, as reflected in the high normalized rate constant obtained.

Notably, the Fe/Au GNCs can be easily detached from the substrate by ultrasonication and dispersed in a liquid. Thus, they have the potential for their use in therapeutic applications, particularly in cancer treatment, due to their ability to generate high levels of ROS. Typically, in Fenton-based cancer treatments, high concentrations of nanoparticles are required to reach high ROS levels in order to be toxic to cancer cells.[62] Additionally, Fenton-based therapies often fail to treat tumors with only the endogenous hydrogen peroxide concentration.[63]

In contrast, Fe/Au nanostructures, which rely on efficient self-supplying H_2O_2 could potentially offer high therapeutic efficiency at very low particle concentrations ($\sim$10 μg mL^{-1}) to produce sufficient local ROS concentrations to kill cancer cells. Additionally, the magnetic character of the iron layer allows for a straightforward magnetic targeting of the tumors.[64,65]

Conclusions

In summary, Fe/Au galvanic nanocells, fabricated using a simple and scalable method, presented excellent degradation performance of persistent organic pollutants by triggering Fenton-like reactions at neutral pH without any additives or external energy sources. One of the key advantages of the Fe/Au nanostructures is the *in situ* formation of H_2O_2, which was detected using a novel adaptation of an H_2O_2-mediated enzymatic reaction. Additionally, the high reducing capability of the Au layer enhances the Fe^{2+}/Fe^{3+} regeneration in the Fenton catalytic loop, minimizing competing and undesirable side reactions that could lead to the fast passivation of the catalyst. The results of the ROS scavenging experiments confirmed hydroxyl radicals as the main reactive oxygen species for pollutant degradation. Compared to the other reported systems, the self-powered galvanic Fenton nanogenerator described here shows enhanced performance for MB and TC degradation (degradation efficiencies of 94% and 72.6%, respectively), with a very small amount of catalyst, at neutral pH and without the need for any additives or external power sources.

In addition, the system has high potential for tuning its reactivity. As it is composed of plasmonic and magnetic materials, the ROS reaction could be further enhanced by locally increasing the temperature through the activation of plasmons using NIR light or by applying alternating magnetic fields.[72,73] In turn, the mass transport of reagents and products could be facilitated by magnetic stirring[74,75] using alternating magnetic fields to induce the rotation of the nanostructures.[76]

The operational conditions of this system, including the neutral pH, the endogenous production of H_2O_2, and the use of a very small amount of catalyst to initiate the process, as well as its magnetoplasmonic capabilities, make the Fe/Au GNCs promising for biomedical applications, such as cancer treatment through ROS therapy.[77–79] For this application, the galvanic Fenton nanogenerators should be surface engineered to control the ROS reaction by using protective coatings, thus enabling the reaction to be activated at the desired time and location. For example, they could be easily coated with different smart molecules, including lipid coatings, various enzymes, or pH-responsive smart molecules, which could also be activated using magnetic/NIR light heating only within a specific tissue region. Therefore, the combination of the galvanic and magneto-plasmonic properties of these nanostructures could open up a wide range of potential applications.

Conflicts of interest

There are no conflicts to declare.

Acknowledgements

G. Shahnazarova would like to acknowledge the PREBIST project, which has received funding from the European Union's Horizon 2020 research and innovation program under the Marie Skłodowska-Curie grant agreement No. 754558. We acknowledge funding from Generalitat de Catalunya through the 2021-SGR-00651 project. We acknowledge the financial support from the Spanish de Ciencia e Innòvacion (MCIIN) through the projects PGC2018-095032-*B*-100, PID2019-106229RB-100 and PID2021-124568NB-I00 funded by MCIN/AEI/10.13039/501100011033. ICN2 is funded by the CERCA program/Generalitat de Catalunya. The ICN2 is supported by the CEX2021-001214-S grant funded by MCIN/AEI/10.13039/501100011033. The authors also acknowledge the Service of Microscopy of UAB (Dr Helena Montón) for their assistance in confocal fluorescence microscopy measurements.

References

1 J. Wu, P. Ning, R. Gao, Q. Feng, Y. Shen, Y. Zhang, Y. Li, C. Xu, Y. Qin, G. R. Plaza, Q. Bai, X. Fan, Z. Li, Y. Han, M. S. Lesniak, H. Fan and Y. Cheng, *Adv. Sci.*, 2020, **7**, 1902933.
2 B. Perillo, M. Di Donato, A. Pezone, E. Di Zazzo, P. Giovannelli, G. Galasso, G. Castoria and A. Migliaccio, *Exp. Mol. Med.*, 2020, **52**, 192–203.
3 X. Xu, J. Wang, T. Chen, N. Yang, S. Wang, X. Ding and H. Chen, *Appl. Catal., B*, 2021, **296**, 120352.
4 Q. Li, J. Ren, Y.-J. Hao, Y.-L. Li, X.-J. Wang, Y. Liu, R. Su and F.-T. Li, *Appl. Catal., B*, 2022, **317**, 121761.
5 B. Jiang, Y. Yao, R. Xie, D. Dai, W. Lu, W. Chen and L. Zhang, *Appl. Catal., B*, 2016, **183**, 291–297.
6 G. Wen, S.-J. Wang, J. Ma, T.-L. Huang, Z.-Q. Liu, L. Zhao and J.-L. Xu, *J. Hazard. Mater.*, 2014, **275**, 193–199.
7 H.-L. Lien and R. Wilkin, *Environ. Sci. Technol.*, 2002, **36**, 4436–4440.
8 A. D. Bokare and W. Choi, *Environ. Sci. Technol.*, 2009, **43**, 7130–7135.
9 P. Zhou, J. Zhang, Y. Zhang, J. Liang, Y. Liu, B. Liu and W. Zhang, *J. Mol. Catal. A: Chem.*, 2016, **424**, 115–120.
10 S. H. Joo, A. J. Feitz and T. D. Waite, *Environ. Sci. Technol.*, 2004, **38**, 2242–2247.
11 H. J. Sung, A. J. Feitz, D. L. Sedlak and T. D. Waite, *Environ. Sci. Technol.*, 2005, **39**, 1263–1268.
12 C. Noubactep, *Environ. Sci. Technol.*, 2009, **43**, 3964–3965.
13 X. Guan, Y. Sun, H. Qin, J. Li, I. M. C. Lo, D. He and H. Dong, *Water Res.*, 2015, **75**, 224–248.
14 T. Phenrat, N. Saleh, K. Sirk, R. D. Tilton and G. V. Lowry, *Environ. Sci. Technol.*, 2007, **41**, 284–290.
15 Q. Jin, J. Kang, Q. Chen, J. Shen, F. Guo and Z. Chen, *Appl. Catal., B*, 2020, **268**, 118453.

16 M. Cheng, C. Lai, Y. Liu, G. Zeng, D. Huang, C. Zhang, L. Qin, L. Hu, C. Zhou and W. Xiong, *Coord. Chem. Rev.*, 2018, **368**, 80–92.
17 Q. Q. Cai, B. C. Y. Lee, S. L. Ong and J. Y. Hu, *Water Res.*, 2021, **190**, 116692.
18 M. Stefaniuk, P. Oleszczuk and Y. S. Ok, *Chem. Eng. J.*, 2016, **287**, 618–632.
19 H. Qin, J. Li, H. Yang, B. Pan, W. Zhang and X. Guan, *Environ. Sci. Technol.*, 2017, **51**, 5090–5097.
20 M. M. Tarekegn, A. M. Hiruy and A. H. Dekebo, *RSC Adv.*, 2021, **11**, 18539–18551.
21 Y. Liu, Y. Zhao and J. Wang, *J. Hazard. Mater.*, 2021, **404**, 124191.
22 X. Nie, J. Liu, D. Yue, X. Zeng and Y. Nie, *Chemosphere*, 2013, **90**, 2403–2407.
23 Z. Zhang, Q. Shen, N. Cissoko, J. Wo and X. Xu, *J. Hazard. Mater.*, 2010, **182**, 252–258.
24 Z. Zhang, Z. Lv, S. A. Baig and X. Xu, *J. Exp. Nanosci.*, 2014, **9**, 603–615.
25 W. J. Liu, T. T. Qian and H. Jiang, *Chem. Eng. J.*, 2014, **236**, 448–463.
26 X. Qin, Z. Wang, C. Guo, R. Guo, Y. Lv and M. Li, *J. Environ. Manage.*, 2022, **306**, 114500.
27 A. Castro, I. Carvalho, L. Marques, P. J. Ferreira, A. Cavaleiro, S. Carvalho and S. Calderon V., *Appl. Surf. Sci.*, 2021, **537**, 147896.
28 S. Luo, S. Yang, C. Sun and J. D. Gu, *Sci. Total Environ*, 2012, **429**, 300–308.
29 Q. Xia, D. Zhang, Z. Yao and Z. Jiang, *Chemosphere*, 2022, **289**, 133195.
30 X. Zhou, G. Jing, B. Lv, Z. Zhou and R. Zhu, *Chemosphere*, 2016, **160**, 332–341.
31 J. Shi, B. Ni, J. Zhang, C. Wu, D. Cheng, Y. Chi, H. Wang, M. Wang and Z. Zhao, *Metals*, 2019, **9**, 341.
32 W. Yang, Q. Wang, W. Li, L. Xue, H. Liu, J. Zhou, J. Mo and B. Shen, *Mater. Des.*, 2019, **161**, 136–146.
33 B. Wei, X. Li, H. Sun, K. Song and L. Wang, *J. Non-Cryst. Solids*, 2021, **564**, 120838.
34 X. Wang, Q. Zhang, S. X. Liang, Z. Jia, W. Zhang, W. Wang and L. C. Zhang, *Catalysts*, 2020, **10**, 48.
35 Q. Wang, M. Chen, P. Lin, Z. Cui, C. Chu and B. Shen, *J. Mater. Chem. A*, 2018, **6**, 10686–10699.
36 S. X. Liang, Q. Zhang, Z. Jia, W. Zhang, W. Wang and L. C. Zhang, *J. Colloid Interface Sci.*, 2021, **581**, 860–873.
37 S. X. Liang, Z. Jia, Y. J. Liu, W. Zhang, W. Wang, J. Lu and L. C. Zhang, *Adv. Mater.*, 2018, **30**, 1802764.
38 Z. Jia, X. Duan, W. Zhang, W. Wang, H. Sun, S. Wang and L. C. Zhang, *Sci. Rep.*, 2016, **6**, 38520.
39 L. Hou, Q. Wang, X. Fan, F. Miao, W. Yang and B. Shen, *New J. Chem.*, 2019, **43**, 6126–6135.
40 Y. Liu, Z. Chen, X. Yang, J. Zhang, Z. Sun, Y. Chen and F. Liu, *J. Mater. Res. Technol.*, 2021, **15**, 256–267.
41 Y. Wu, Q. Yue, Y. Gao, Z. Ren and B. Gao, *J. Environ. Sci.*, 2018, **69**, 173–182.
42 J. Duan, H. Zhu, F. Xu and J. Zhao, *Chem. Eng. J.*, 2016, **304**, 282–288.
43 L. Soler and S. Sánchez, *Nanoscale*, 2014, **6**, 7175–7182.
44 X. Ruan, H. Liu, X. Ning, D. Zhao and X. Fan, *Sci. Total Environ*, 2020, **715**, 136822.
45 J. F. Gao, Z. L. Wu, W. J. Duan and W. Z. Zhang, *Sci. Total Environ*, 2019, **662**, 978–989.
46 S. Zhang, D. Wang, L. Zhou, X. Zhang, P. Fan and X. Quan, *Chem. Eng. J.*, 2013, **217**, 99–107.
47 M. L. Tran, C. H. Nguyen, T. T. V. Tran and R. S. Juang, *J. Taiwan Inst. Chem. Eng.*, 2020, **111**, 130–140.
48 C. H. Nguyen, M. L. Tran, T. T. V. Tran and R. S. Juang, *J. Taiwan Inst. Chem. Eng.*, 2021, **119**, 80–89.
49 H. H. Girault. *Analytical and Physical Electrochemistry*, EPFL Press/Marcel Dekker, New York, 2004.
50 R. F. P. Nogueira, M. C. Oliveira and W. C. Paterlini, *Talanta*, 2005, **66**, 86–91.
51 Y. Nosaka and A. Y. Nosaka, *Chem. Rev.*, 2017, **117**, 11302–11336.
52 T. V. Votyakova and I. J. Reynolds, *J. Neurochem.*, 2001, **79**, 266–277.
53 C. C. A. Loures, M. A. K. Alcântara, H. J. Izário Filho, A. C. S. C. Teixeira, F. T. Silva, T. C. B. Paiva and G. R. L. Samanamud, *Int. Rev. Chem. Eng.*, 2013, **5**, 102.
54 M. Bayat, B. Nasernejad and C. Falamaki, *Sci. Rep.*, 2021, **11**, 7715.
55 I. Khan, K. Saeed, I. Zekker, B. Zhang, A. H. Hendi, A. Ahmad, S. Ahmad, N. Zada, H. Ahmad, L. A. Shah, T. Shah and I. Khan, *Water*, 2022, **14**, 242.
56 A. Fiaz, D. Zhu and J. Sun, *Environ. Sci. Eur.*, 2021, **33**, 64.
57 W. Ye, J. Lu, J. Ye and Y. Zhou, *J. Cleaner Prod.*, 2021, **278**, 123567.
58 M. Chen, Y. Wu, Y. Han, X. Lin, J. Sun, W. Zhang and R. Cao, *ACS Appl. Mater. Interfaces*, 2015, **7**, 21852–21859.
59 R. L. Doyle and M. E. G. Lyons, *Phys. Chem. Chem. Phys.*, 2013, **15**, 5224–5237.
60 L. J. Enman, A. E. Vise, M. B. Stevens and S. W. Boettcher, *ChemPhysChem*, 2019, **20**, 3089–3095.
61 M. E. G. Lyons and R. L. Doyle, *Int. J. Electrochem. Sci.*, 2012, **7**, 9488–9501.
62 C. Xu, Z. Yuan, N. Kohler, J. Kim, M. A. Chung and S. Sun, *J. Am. Chem. Soc.*, 2009, **131**, 15346–15351.
63 F. Paquin, J. Rivnay, A. Salleo, N. Stingelin and C. Silva, *J. Mater. Chem. C*, 2015, **3**, 10715–10722.
64 Z. Li, A. Aranda-Ramos, P. Güell-Grau, J. L. Tajada, L. Pou-Macayo, S. Lope Piedrafita, F. Pi, A. G. Roca, M. D. Baró, J. Sort, C. Nogués, J. Nogués and B. Sepúlveda, *Appl. Mater. Today*, 2018, **12**, 430–440.
65 A. Fluksman, A. Lafuente, Z. Li, J. Sort, S. Lope-Piedrafita, M. J. Esplandiu, J. Nogues, A. G. Roca, O. Benny and B. Sepulveda, *ACS Nano*, 2022, **17**, 1946–1958.
66 C. Lu, W. Sun, T. Yue, H. Han, W. Yu, A. V. Nguyen and L. Wang, *J. Hazard. Mater.*, 2020, **400**, 123210.
67 J. Liu, Y. Du, W. Sun, Q. Chang and C. Peng, *RSC Adv.*, 2019, **9**, 22513–22522.
68 B. Wei, X. Li, H. Sun, K. Song and L. Wang, *J. Non. Cryst. Solids*, 2022, **575**, 121212.
69 M. Ayoub, *Water Pract. Technol.*, 2022, **17**, 246–253.

70 Y. Liu, C. Wang, Z. Sui and D. Zou, *Sep. Purif. Technol.*, 2018, **203**, 29–35.
71 Y. Jiang, D. Sun, D. Wang, L. Tong, Z. Zhang, N. Cao and Z. Gong, *Environ. Technol.*, 2022, **43**, 3719–3727.
72 Z. Tang, P. Zhao, H. Wang, Y. Liu and W. Bu, *Chem. Rev.*, 2021, **121**, 1981–2019.
73 L. Shi, X. Wang, Y. Hu and Y. He, *Sol. Energy*, 2020, **196**, 505–512.
74 A. Serrà, M. Montiel, E. Gómez and E. Vallés, *Nanomaterials*, 2014, **4**, 189–202.
75 A. Serrà, S. Grau, C. Gimbert-Suriñach, J. Sort, J. Nogués and E. Vallés, *Appl. Catal., B*, 2017, **217**, 81–91.
76 Z. Li, A. Lopez-Ortega, A. Aranda-Ramos, J. L. Tajada, J. Sort, C. Nogues, P. Vavassori, J. Nogues and B. Sepulveda, *Small*, 2018, **14**, 1800868.
77 Y. Li, P. Zhao, T. Gong, H. Wang, X. Jiang, H. Cheng, Y. Liu, Y. Wu and W. Bu, *Angew. Chem., Int. Ed.*, 2020, **59**, 22537–22543.
78 S. Wang, Z. Wang, Z. Li, X. Zhang, H. Zhang, T. Zhang, X. Meng, F. Sheng and Y. Hou, *Sci. Adv.*, 2022, **8**, DOI: **10.1126/sciadv.abn3883**.
79 J. Wang, Z. Sun, S. Wang, C. Zhao, J. Xu, S. Gao, M. Yang, F. Sheng, S. Gao and Y. Hou, *J. Am. Chem. Soc.*, 2022, 19884–19895.

